ADVANCED FUNCTIONAL MATERIALS
www.afm-journal.de

Iodine Electrochemistry Dictates Voltage-Induced Halide Segregation Thresholds in Mixed-Halide Perovskite Devices

Zhaojian Xu, Ross A. Kerner, Joseph J. Berry, and Barry P. Rand**

Owing to straightforward stoichiometry–bandgap tunability, mixed-halide perovskites are ideal for many optoelectronic devices. However, unwanted halide segregation under operational conditions, including light illumination and voltage bias, restricts practical use. Additionally, the origin of voltage-induced halide segregation is still unclear. Herein, a systematic voltage threshold study in mixed bromide/iodide perovskite devices is performed and leads to observation of three distinct voltage thresholds corresponding to the doping of the hole transport material (0.7 ± 0.1 V), halide segregation (0.95 ± 0.05 V), and degradation (1.15 ± 0.05 V) for an optically stable mixed-halide perovskite composition with a low bromide content (10%). These empirical threshold voltages are minimally affected by composition until very Br-rich compositions, which reveals the dominant role of iodide/triiodide/iodine electrochemistry in voltage-induced Br/I phase separation and transport layer doping reactions in halide perovskite devices.

1. Introduction

Metal halide perovskites have been widely implemented in optoelectronic devices in the past decade, attracting considerable attention.[1–4] One promising characteristic of metal halide perovskites is that the bandgap can be easily tuned by varying stoichiometry of the halide sublattice (e.g., I^-, Br^-, and Cl^-),[5,6] with proposed applications as color-tunable light emitters[5,7] and as wide-bandgap sub-cells for perovskite-based tandem solar cells.[8–10] However, a considerable breadth of mixed-halide perovskite stoichiometry range is unstable under light illumination and suffers from light-induced halide segregation.[11–13] Further studies have shown such halide segregation can also occur under voltage bias stress,[14–16] affecting both solar cells and light-emitting diodes, making this phenomenon a concern for all foreseen perovskite-based electronic device applications. While light-induced halide segregation has been heavily studied, voltage-induced halide segregation still lacks in-depth investigation. For example, for light-induced halide segregation, it has been reported that there is a critical bromide ratio in $MAPb(Br_xI_{1-x})_3$ (MA, methylammonium; where x denotes the bromide fraction of total halides species) at $x = 0.2$,[11] and only compositions with $x > 0.2$ show halide segregation under light illumination, while the compositions with $x < 0.2$ are optically stable. However, whether there is a similar critical halide stoichiometry for voltage-induced halide segregation is still unclear.

In earlier work, we proposed a photoelectrochemical model to rationalize both light-induced and voltage-induced halide segregation, where we assumed that halide segregation is initiated by the oxidation of the most easily oxidized halide species and enabled by the asymmetry or spatial inhomogeneity in the thermodynamic (light illumination and voltage bias) and kinetic (concentration gradient, reaction rate, and spatial inhomogeneity) driving forces.[17] In the case of voltage-induced halide segregation viewed from an electrochemical perspective, the application of voltage bias provides the thermodynamic driving force asymmetry via spatial separation of the oxidation and reduction reactions localized at the anode and cathode, respectively. Voltage thresholds for halide segregation have not been systematically studied, yet are critical for understanding the origins of voltage-induced halide segregation. Importantly, the voltage thresholds for halide segregation and degradation determine the stability window of perovskite-based devices, and it is necessary to understand the impact of voltage bias and identify

Z. Xu, B. P. Rand
Department of Electrical and Computer Engineering
Princeton University
Princeton, NJ 08544, USA
E-mail: brand@princeton.edu
R. A. Kerner, J. J. Berry
National Renewable Energy Laboratory
Golden, CO 80401, USA
E-mail: joe.berry@nrel.gov
J. J. Berry
Renewable and Sustainable Energy Institute
University of Colorado Boulder
Boulder, CO 80309, USA
J. J. Berry
Department of Physics
University of Colorado Boulder
Boulder, CO 80309, USA
B. P. Rand
Andlinger Center for Energy and the Environment
Princeton University
Princeton, NJ 08544, USA

The ORCID identification number(s) for the author(s) of this article can be found under https://doi.org/10.1002/adfm.202203432.

DOI: 10.1002/adfm.202203432

potential electrochemical reactions and their voltage thresholds to ensure devices always operate within the stability window and, further, to establish strategies that increase these thresholds.

In this work, we systematically study the impact of voltage bias in model n-i-p devices consisting of fluorine-doped tin oxide (FTO)/MAPb(Br_xI_{1-x})$_3$/undoped 2,2′,7,7′-tetrakis(N,N-di-*p*-methoxyphenylamino)-9,9′-spirobifluorene (spiro-MeOTAD)/Au across the full range of Br/I ratios by conducting a series of long-time voltage biasing tests. By combining current density transient measurements, current density-voltage (*J–V*) characteristics, and photoluminescence (PL) spectra, we confirm three voltage thresholds for an optically stable, mixed-halide perovskite composition with a low bromide ratio ($x = 0.1$), and assign them, in order of increasing voltage, as the spiro-MeOTAD doping threshold (0.7 ± 0.1 V), halide segregation threshold (0.95 ± 0.05 V), and degradation threshold (1.15 ± 0.05 V), respectively. This indicates that unlike light-induced halide segregation, all mixed-halide compositions can be vulnerable to voltage-induced halide segregation regardless of the halide ratio. Finally, by changing the Br/I ratio used in the structure, we explore how these voltage thresholds vary across halide composition and establish the stability window for these compositions, which provides an operational guideline for perovskite-based electronic devices. Our results unequivocally confirm that, as expected based on relative reduction/oxidation potentials, iodide/triiodide/iodine dictate the minimum voltage thresholds in mixed bromide/iodide perovskite devices.

2. Results

Figure 1a,b and Figure S1 (Supporting Information) show the device structure and schematic of the measurement used to extract the voltage thresholds for pure iodide, pure bromide, and mixed-halide perovskite layers. In a typical measurement, we bias the device at a constant voltage for 12 h recording current density as a function of time (*J–t*), and compare the *J–V* curves and PL spectra before and after biasing. According to the electrochemical model we proposed for halide segregation,[17] the voltage-induced halide segregation in mixed bromide/iodide perovskite is initiated by iodide oxidation at the anode. We have also demonstrated that spiro-MeOTAD can be doped by iodine sourced from I_2 vapor as well as released from the perovskite layer, resulting in increased conductivity, and displaying fast iodine/triiodide permeation rates.[18] In the device structure probed here, we exploit the ease of measuring conductivity changes in the initially undoped spiro-MeOTAD, taking it as an indicator for iodide released from the perovskite layer. Once liberated, iodine/triiodide/iodide within the spiro-MeOTAD is much more mobile, capable of migrating vertically and laterally to influence many observables including halide segregation. Below, we begin by determining thresholds for pure $MAPbI_3$ and $MAPbBr_3$ perovskites before characterizing halide segregation in $x = 0.1$ composition, followed by threshold determinations for the full range of x.

2.1. Pure Halide Compositions ($x = 0$ and $x = 1$): Spiro-MeOTAD Doping Thresholds

We start the voltage threshold study from two single-halide compositions, pure iodide ($x = 0$) and pure bromide ($x = 1$). For $MAPbI_3$, when we increase the bias voltage in 0.1 V increments from 0.6 V, we observe current density increases with time when 0.8 V or more is applied. The current increase observed in *J–t* measurement is further corroborated by comparing the *J–V* characteristics before and after long-time voltage biasing (Figure S2, Supporting Information) where we observe that the current at a large forward bias (2 V) also increases after biasing the device at 0.8 V for 12 h. We interpret this as an indication of spiro-MeOTAD doping by iodide or triiodide permeating into the spiro-MeOTAD layer.[18,19]

To demonstrate the doping of spiro-MeOTAD by iodine species in a $MAPbI_3$ device, we compare cross-sectional scanning transmission electron microscopy–energy dispersive X-ray spectroscopy (STEM-EDX) measurements on an unbiased (control) $MAPbI_3$ device and a $MAPbI_3$ device biased at 1.0 V for 12 h, as shown in Figure 1d,e. From high-angle annular dark field (HAADF) STEM images, we can clearly see a distinct region at $MAPbI_3$/spiro-MeOTAD interface in both control and biased devices, and the biased device shows a thicker interfacial layer than the control device. The elemental distribution from EDX line scan and EDX maps (Figure S3 and S4, Supporting Information) further reveal that the interfacial layer consists of iodine species, alone (no Pb), permeating into the spiro-MeOTAD layer as indicated by the red arrow. Furthermore, Figure 1f shows I 3d X-ray photoelectron spectroscopy (XPS) measurements on unbiased (control) devices and devices biased at various voltages (after peeling off the top Au electrode with tape), and we find enhanced I 3d intensity after biasing the device at 0.7 V for 12 h, while C 1s spectra (Figure S5, Supporting Information) change negligibly. Further quantitative analysis shown in Figure S5 in the Supporting Information also confirms enriched iodine species in the spiro-MeOTAD layer. Both STEM–EDX and XPS results demonstrate that spiro-MeOTAD can be spontaneously doped by iodine species in an unbiased device to a limited extent, while voltage-induced doping of spiro-MeOTAD occurs when the bias voltage exceeds a certain value. Based on *J–t, J–V,* and XPS results, we thus assign the first voltage threshold observed in the $MAPbI_3$ device as the spiro-MeOTAD doping threshold, and determine it to be 0.7 ± 0.1 V (a more detailed discussion about determining this threshold value is described in Figure S2 in the Supporting Information).

For $MAPbBr_3$, we find the current transient does not increase until 1.2 V (Figure 1g and Figure S6, Supporting Information). Since there is no iodine species in the $MAPbBr_3$ device, we interpret this as spiro-MeOTAD doping by bromine species permeating into the spiro-MeOTAD layer. Figure 1h,i shows the cross-sectional STEM-EDX measurements on an unbiased device and a device biased at 1.4 V for 12 h, where we observe a similar interfacial layer formed by the penetration of bromine species into the spiro-MeOTAD layer, which is also confirmed by EDX maps (Figures S7 and S8, Supporting Information) as well as Br 3d (Figure 1j) and C 1s (Figure S9, Supporting Information) XPS measurements similarly showing voltage-induced bromine enrichment in the spiro-MeOTAD layer at voltages above the *J–t*-derived threshold. These measurements unambiguously demonstrate spiro-MeOTAD is also doped by bromine species, but at a much higher voltage bias compared to iodine species. Combining *J–t, J–V,* and XPS results, we thus determine the spiro-MeOTAD doping threshold in $MAPbBr_3$ to

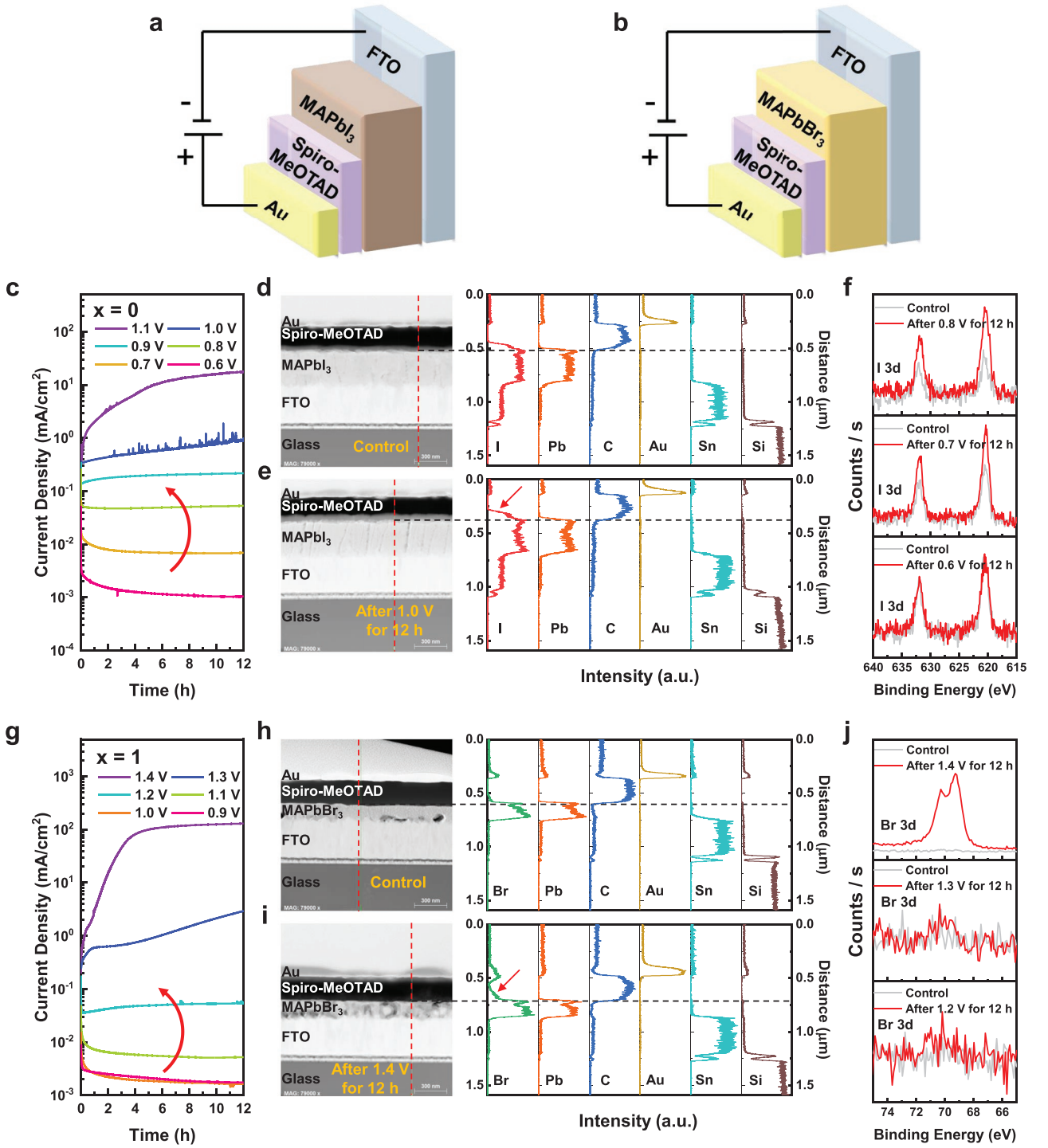

Figure 1. Device structure of the voltage stressing test to extract the voltage thresholds for a) $MAPbI_3$ and b) $MAPbBr_3$. Determination of the spiro-MeOTAD doping thresholds in c-f) $MAPbI_3$ and g-j) $MAPbBr_3$ devices. Current transients at various voltages over 12 h for c) $MAPbI_3$ and g) $MAPbBr_3$ devices. Cross-sectional HAADF STEM images and EDX elemental distributions for d) unbiased (control) $MAPbI_3$ devices, e) biased (at 1.0 V for 12 h) $MAPbI_3$ devices, h) unbiased (control) $MAPbBr_3$ devices, and i) biased (at 1.4 V for 12 h) $MAPbBr_3$ devices. The red and black dash lines in STEM images mark the line used for EDX measurements and the perovskite/spiro-MeOTAD interface, respectively, in the elemental depth profiles (to the right of STEM images). XPS spectra of unbiased (control) and biased f) $MAPbI_3$ (I 3d) and j) $MAPbBr_3$ (Br 3d) devices at various voltages after peeling off the top Au electrode.

be 1.1 ± 0.1 V (a more detailed discussion about determining this threshold value is described in Figure S6 in the Supporting Information).

2.2. Pure Halide Compositions ($x = 0$ and $x = 1$): Degradation Thresholds

In addition to the spiro-MeOTAD doping threshold established above, we further determine the degradation thresholds for $MAPbI_3$ and $MAPbBr_3$, where we term "degradation" the irreversible structural change and decomposition of the perovskite layer, to establish the upper limit to the voltage stability window. **Figure 2** shows the data collected to quantify the degradation thresholds primarily relying on PL spectroscopy corroborated by scanning electron microscopy (SEM) and X-ray diffraction (XRD). For $MAPbI_3$, we observe that the PL spectrum of the active region is unaltered for voltage biases up to 1.1 V, but, at 1.2 V, the PL spectrum begins to blueshift compared to the initial spectrum (Figure 2a–c, indicated by the green arrows, and Figure S2, Supporting Information). Accompanying the PL blueshift, the active region also becomes visibly darkened when the biasing voltage exceeds 1.2 V as shown in the inset photos in Figure 2a–c. Since $MAPbI_3$ is a pure halide composition, the PL shift observed here is obviously not due to halide segregation. Previously, a PL blueshift has been reported as a sign of degradation in $MAPbI_3$,[20] and we have also determined the degradation threshold to be 1.2 V for $MAPbI_3$ in this structure via time of flight secondary ion mass spectroscopy (TOF-SIMS) and STEM-EDX measurements in our previous work.[19] To further confirm the degradation of $MAPbI_3$, we picked an unbiased (control) device and a device biased at 1.5 V for 12 h, peeled off the top Au electrode with tape, and removed spiro-MeOTAD by washing with chlorobenzene (CB) to expose the $MAPbI_3$ layer. Figure 2d,e,f, and Figure S10a (Supporting Information) show SEM, XRD, and ultraviolet-visible (UV-vis) absorption spectra measurements of the control and biased $MAPbI_3$ layer. The biased sample shows worse morphology, decreased XRD intensity, and enhanced scattering. All of these results indicate the degradation of the perovskite layer. Thus, we assign this voltage threshold (1.15 ± 0.05 V) as the degradation threshold for $MAPbI_3$ and demonstrate that PL blueshift in the absence of halide segregation is an effective indicator for degradation.

For $MAPbBr_3$, we find the PL to blueshift at 1.3 V (Figure 2g–i, indicated by the green arrows; and Figure S6, Supporting Information), accompanied by a similar darkening of the active region. We then carried out similar SEM (Figure 2j,k), XRD (Figure 2l) and UV-vis absorption (Figure S10b, Supporting Information) measurements on a biased $MAPbBr_3$ device (biased at 1.5 V for 12 h) compared with an unbiased device. The worse morphology accompanied by lower XRD intensity for the biased sample mirrors the case of degraded $MAPbI_3$. Thus, via the same rationale, we determine the degradation threshold for $MAPbBr_3$ to be 1.25 ± 0.05 V in this device structure.

Establishing these degradation thresholds places an upper bound on the voltage stability windows of the devices for long-term operation, above which the changes to device characteristics are dominated by non-negligible consumption of MAX (X, halide anion) and detrimental reactions. We acknowledge that using PL blueshifts to determine the degradation threshold of mixed-halide perovskites ($0 < x < 1$) is not always reliable, since halide segregation may also induce a PL blueshift due to the formation of Br-rich regions (see next section). However, we assume that the degradation threshold of mixed-halide perovskites will not exceed that of the pure I or Br compositions.

2.3. Optically Stable Mixed-Halide Composition ($x = 0.1$)

We performed the same set of measurements on a mixed bromide/iodide perovskite with low bromide ratio ($x = 0.1$), one which is optically stable and immune to light-induced halide segregation confirmed by PL transient measurements (Figure S11, Supporting Information), so that we can exclude any interference from light-induced halide segregation during the PL measurement. **Figure 3**a shows the J–t curves of $MAPb(Br_{0.1}I_{0.9})_3$ biased at the indicated voltages for 12 h which reveal two thresholds below the onset of degradation. First, we observe a similar spiro-MeOTAD doping threshold as established in pure-halide compositions. We find current density increases with time when 0.8 V or more is applied, which is also confirmed by comparing the J–V characteristics before and after extended voltage biasing (Figure S12, Supporting Information). Additionally, I 3d (Figure 3b) and C 1s (Figure S13, Supporting Information) XPS measurements on unbiased (control) devices and devices biased at various voltages (after peeling off the top Au electrode) also reveal an enhanced I 3d/C 1s peak area ratio after biasing the device at 0.7 V for 12 h, which confirms the doping of spiro-MeOTAD by iodine species. Thus, the threshold for spiro-MeOTAD doping for $x = 0.1$ is also 0.7 ± 0.1 V, unchanged from the threshold for $MAPbI_3$.

Upon increasing the bias voltage by 0.1 V increments, we observe that the PL spectrum redshifts after 1.0 V (Figure 3c,d, indicated by a red arrow). The redshift of the PL spectrum has been reported previously and understood as an indication of the formation of I-rich domains (i.e., halide segregation) for both light-induced and voltage-induced halide segregation.[11,12,14] Therefore, we assign the voltage range 0.95 ± 0.05 V as the threshold for voltage-induced halide segregation. Furthermore, the red-shifted PL almost recovered after 24 h in the dark, indicating that voltage-induced halide segregation is partially reversible as long as the degradation threshold is not exceeded (Figure S14, Supporting Information). It is worth noting that the critical bromide ratio for light-induced halide segregation is around $x = 0.2$,[11] and only compositions with $x > 0.2$ show halide segregation under light illumination, while the compositions with $x < 0.2$ are observed to be optically stable (Figure S11, Supporting Information). Interestingly, here we observe that voltage-induced halide segregation can occur even for an optically stable composition ($x = 0.1$).

Finally, the third voltage threshold (degradation) was observed between 1.1–1.2 V, where blue-shifted components emerge in the PL spectra after biasing (Figure 3e,f, indicated by a green arrow). These blue-shifted components are consistent with what we observed in the case of pure-halide perovskites beyond the degradation threshold, and these blue-shifted PL components do not recover even after 60 h in the dark (Figure S14, Supporting Information), owing to irreversible

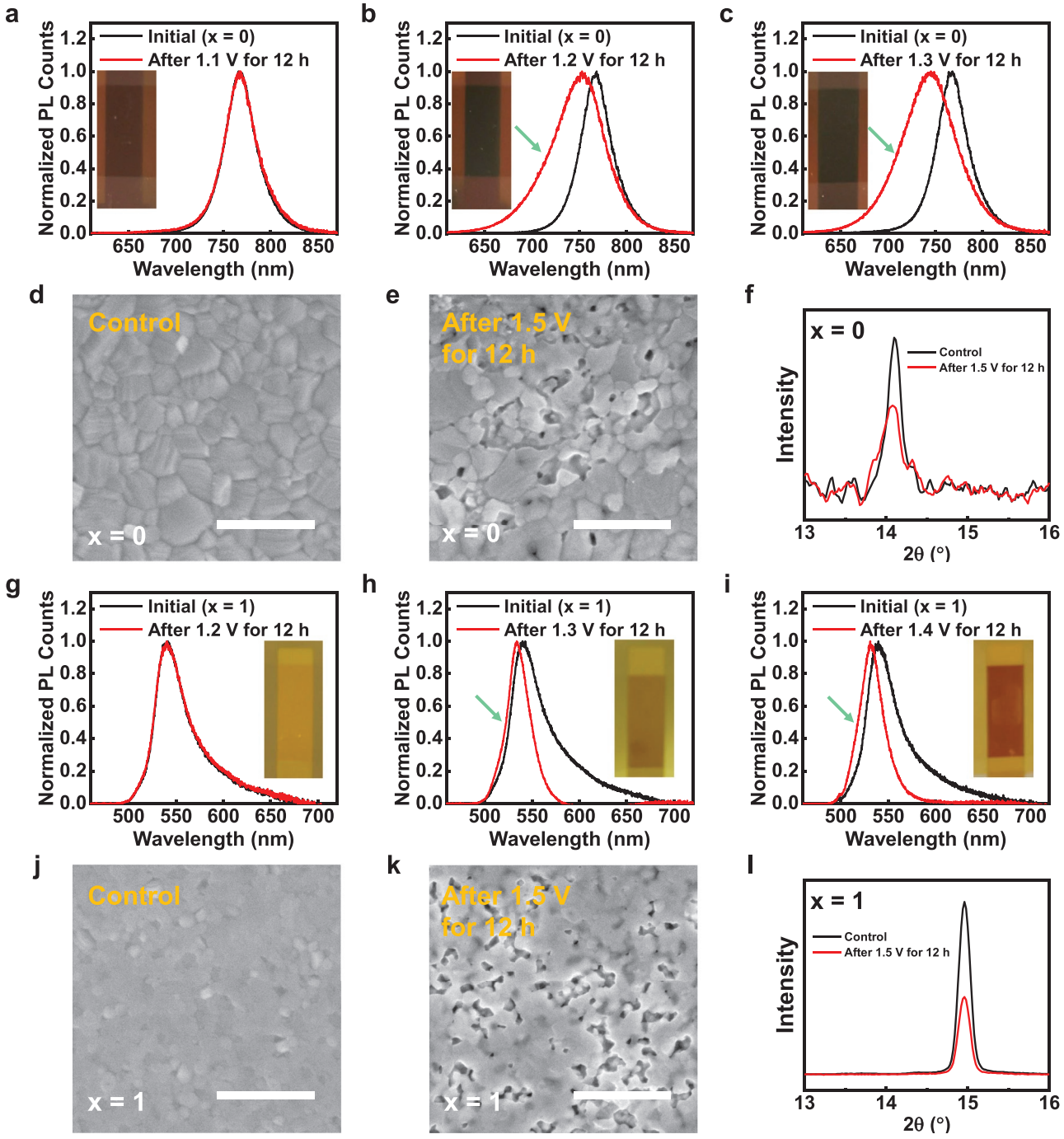

Figure 2. Determination of the degradation thresholds in a–f) $MAPbI_3$ and g–l) $MAPbBr_3$ devices. PL spectra before and after 12 h biasing at various voltages for c–e) $MAPbI_3$ and g–i) $MAPbBr_3$ devices. Inset photos in PL spectra show the active region (0.1 cm^2, 2 × 5 mm) after the voltage biasing test. SEM images for d) unbiased (control) $MAPbI_3$ devices, e) biased (at 1.5 V for 12 h) $MAPbI_3$ devices, j) unbiased (control) $MAPbBr_3$ devices, and k) biased (at 1.5 V for 12 h) $MAPbBr_3$ devices after peeling off the top Au electrode and removing the spiro-MeOTAD layer. Scale bar, 1 µm. XRD patterns of unbiased (control) and biased (at 1.5 V for 12 h) f) $MAPbI_3$ and l) $MAPbBr_3$ devices after peeling off the top Au electrode and removing the spiro-MeOTAD layer.

degradation creating isolated regions of the film. Thus, we assign this voltage as the degradation threshold for mixed-halide compositions. The three voltage thresholds for the FTO/$MAPb(Br_{0.1}I_{0.9})_3$/spiro-MeOTAD/Au device are summarized in Figure 3g, which sets the stability window for device operation and the degradation window that should be avoided.

2.4. Effects of Halide Stoichiometry on Thresholds

To further understand the mechanism of voltage-induced halide segregation and explore voltage thresholds across the Br/I stoichiometry range, we conducted extended biasing tests on compositions systematically varying the x values. We

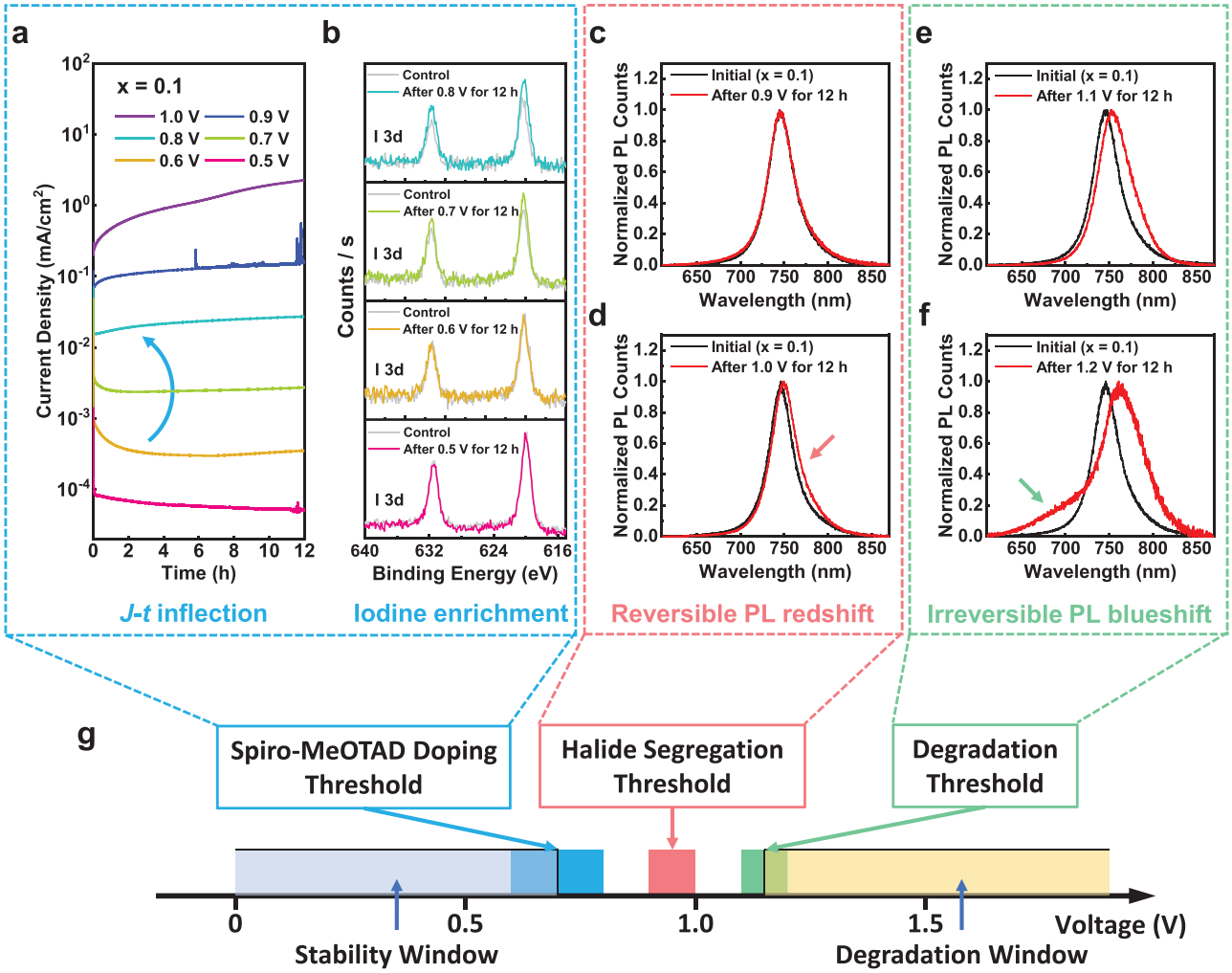

Figure 3. Determination of the voltage thresholds for $MAPb(Br_{0.1}I_{0.9})_3$. a) Current transients at various voltages over 12 h. b) I 3d XPS spectra of unbiased (control) and biased devices at various voltages after peeling off the top Au electrode. (c–f) PL spectra before and after voltage biasing at c) 0.9 V, d) 1.0 V, e) 1.1 V and f) 1.2 V. g) Schematic diagram of voltage thresholds observed in an FTO/$MAPb(Br_{0.1}I_{0.9})_3$/spiro-MeOTAD/Au structure.

changed the solvent for the precursor solution from *N,N*-dimethylformamide (DMF) to dimethyl sulfoxide (DMSO) for bromide-rich compositions to ensure good solubility (bromide salts display much lower solubility in DMF compared to iodide salts) for suitable film thickness and morphologies. Therefore, to avoid any complications from perovskite morphology and layer thickness, we divide samples into two panes in **Figure 4** – iodide-rich compositions ($0 \leq x \leq 0.6$, processed from DMF) and bromide-rich compositions ($0.8 \leq x \leq 1.0$, processed from DMSO) – where the perovskite morphology and layer thickness are consistent for the samples within each group confirmed by top-view SEM measurements on perovskite films (Figure S15, Supporting Information) and cross-sectional SEM measurements on devices (Figure S16, Supporting Information). We performed the same analysis combining *J–t*, *J–V* and PL measurements to extract the voltage thresholds for each composition (detailed data and methods to extract voltage thresholds for each composition are described in Figures S2,S6,S12, and S17–S21 in the Supporting Information). The results are summarized in Figure 4 and the main observations and conclusions for different thresholds are discussed below:

i) The spiro-MeOTAD doping threshold remains relatively constant (0.7 ± 0.1 V) for iodide-rich compositions ($x \leq 0.4$) and increases with an increased ratio of bromide for bromide-rich compositions ($x \geq 0.8$). Notably, there is a dramatic difference in the threshold voltage between a pure-bromide composition ($x = 1$) and a composition with only 1% iodide ($x = 0.99$). This means that even a small loading of iodide strongly influences the spiro-MeOTAD doping threshold, and it indicates the threshold voltages for mixed-halide perovskites are primarily determined by iodine electrochemistry.[21,22] We suspect that iodine-related interstitial defects, which are more numerous for iodide-rich compositions, are the primary species giving rise to spiro-MeOTAD doping at these low voltages and that lattice halides are not yet involved in any reactions.[23]
ii) The halide segregation threshold remains relatively constant at 0.95 ± 0.05 V across the entire iodide-rich Br/I stoichiometry

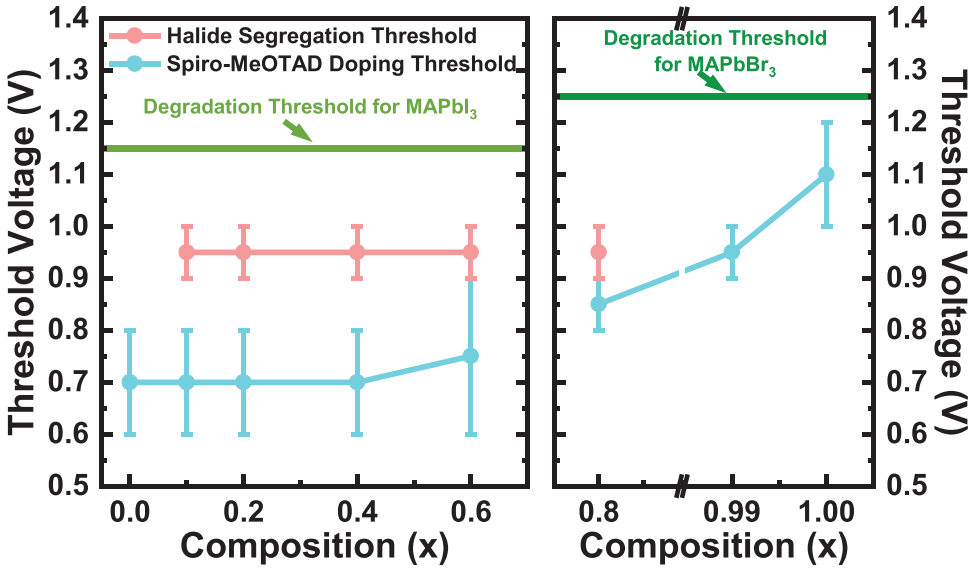

Figure 4. Voltage thresholds determined in FTO/MAPb(Br_xI_{1-x})$_3$/spiro-MeOTAD/Au structure with iodide-rich (left panel, $0 \le x \le 0.6$, processed from DMF) and bromide-rich (right panel, $0.8 \le x \le 1.0$, processed from DMSO) perovskite compositions. The compositions with $x > 0.8$ are too dilute in iodide to show a PL redshift corresponding to halide segregation, and thus are not included in this threshold value.

range. It is possible that lattice halides, in addition to interstitial defects, begin participating in electrochemical reactions at these voltages which are only slightly below the bulk degradation threshold, and methylammonium deprotonation does not yet onset (i.e., degradation has not been activated). It is also worth noting that voltage-induced halide segregation can occur in all mixed-halide compositions, even including an optically stable one ($x = 0.1$), and there appears to be no composition resistant to voltage-induced halide segregation which can be explained by the fact that the mechanism of electrochemical halide oxidation is fundamentally different from photochemical oxidation. This finding is of great significance, especially for the community of perovskite photovoltaics, because a number of high-efficiency single-junction perovskite solar cells[24–27] and most reported wide-bandgap perovskite sub-cells in tandem structures,[8–10] employ mixed-halide perovskite active layers. Although those mixed-halide perovskites used in solar cells are designed to be optically stable and immune to light-induced halide segregation, it should be realized that they are still vulnerable to voltage-induced halide segregation once the voltage bias exceeds the halide segregation threshold, which can be lower than open-circuit voltage or, more alarmingly, very near the maximum power point voltage.

iii) The degradation threshold is reached when methylammonium and lattice halides simultaneously participate in cathodic and anodic reactions, respectively, resulting in a consumption of MAX and irreversible degradation. Notably, the blue-shifted PL due to degradation can be easily mistaken for a halide-segregation-induced PL shift, especially for bromide-rich compositions ($0.4 \le x \le 0.99$). To avoid any potential ambiguity, we restrict our assignment of degradation threshold for the two pure-halide compositions, that of pure-iodide (1.15 ± 0.05 V) and pure-bromide (1.25 ± 0.05 V), in Figure 4, but offer additional discussion and speculation on degradation thresholds for all compositions in Figures S2, S6, S12, and S17–S21 in the Supporting Information.

3. Discussion

3.1. Halide Segregation Mechanism

Iodide has a lower oxidation potential than bromide,[28] so it is expected that iodide will always be oxidized prior to bromide in the presence of both halides. This difference is experimentally supported by the spiro-MeOTAD doping thresholds we observe in Figure 1, and leads us to conclude iodide/triiodide/iodine reactions occur at a faster rate at lower voltages than bromide/tribromide/bromine in our device. We previously discussed voltage-induced halide segregation arising from preferential iodide oxidation at the anode (the spiro-MeOTAD interface in our device), conversion to an oxidized iodine species, and subsequent vertical diffusion or migration of those species to the cathode where they are reduced and re-enter the lattice.[17] This particular mass transport "circuit" (or redox shuttle) and corresponding anodic and cathodic reactions are shown in **Figure 5** (pathways 1–3) and predicts iodide-rich domains should form near the cathode interface. However, our general electrochemical model must be re-evaluated to incorporate several unique aspects of the exact system under investigation: at least one ion permeable contact layer, ambipolar electronic conduction by the perovskite, spatial inhomogeneity in majority carrier type, and spatial distribution of device defects like pinholes.

The device architecture used in this study, as for many perovskite studies, employs an organic hole transport material (HTM) with a relatively shallow highest occupied molecular orbital (HOMO). We know from previous studies that iodine reacts with such HTMs and permeates them quickly, adding complexity to the expected outcomes via additional mass transport pathways and a greater degree of vertical and lateral inhomogeneity. It is also important to note the fact that triiodide/iodide permeates the spiro-MeOTAD layer in relatively large amounts and diffuses through organic hole transport materials on the time scale of seconds.[18] Thus, it can be expected

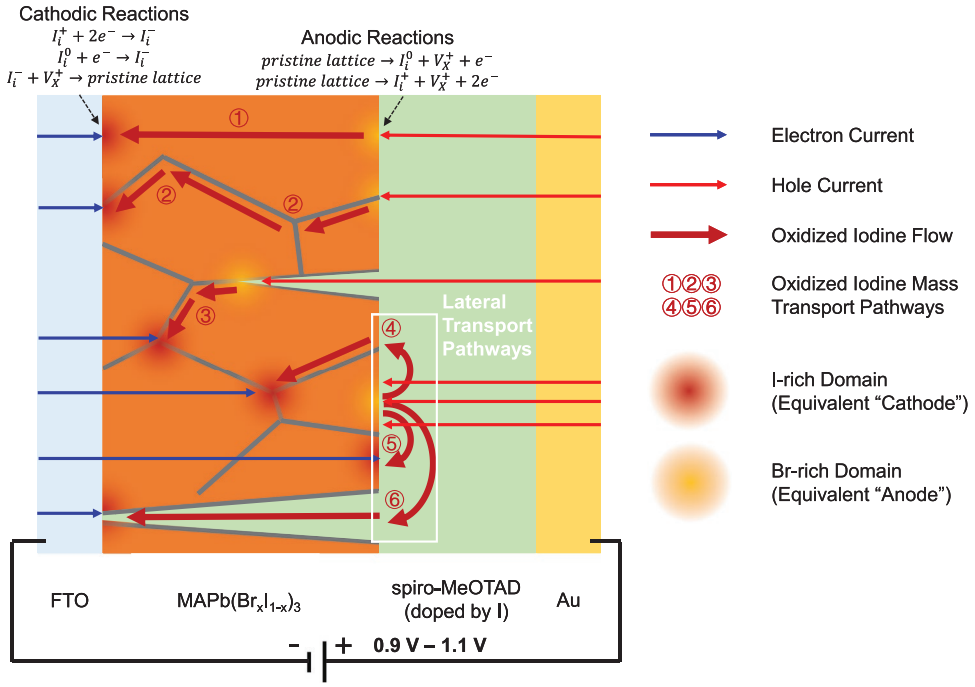

Figure 5. Schematic of voltage-induced halide segregation and possible mass transport pathways of oxidized iodine species in an FTO/$MAPb(Br_xI_{1-x})_3$/spiro-MeOTAD/Au structure. Among other spatial inhomogeneities, this picture accounts for organic HTMs enabling rapid transport of iodine where lateral migration through this layer (mechanisms highlighted by the white box) will influence halide redistribution induced by voltage or illumination.

that iodide released into the spiro-MeOTAD layer becomes the most mobile species in the system and can travel a larger lateral distance before being reincorporated into the perovskite. The impact of this permeable contact layer is illustrated by pathways 4–6 in Figure 5 where iodide/iodine travels laterally before interacting again with the perovskite. In pathway 4, the oxidized iodine species interacts with a p-type region of the perovskite where it can follow the fast vertical transport pathway at a grain boundary-dense region. However, in pathway 5, it encounters a region of the perovskite conducting electrons, and is reduced to possibly enter the halide sublattice again. Finally, pathway 6 shows the iodine within the spiro-MeOTAD layer encountering a major film defect, a pinhole, where it is reduced directly at the FTO without having to transport through the perovskite.

The most unique aspect of Figure 5 highlights lateral flux of iodine within the spiro-MeOTAD layer. We corroborate this with an experiment on an FTO/$MAPb(Br_{0.2}I_{0.8})_3$/poly(9-vinylcarbazole) (PVK)/Au structure where spiro-MeOTAD is replaced with PVK, which is a deep HOMO organic HTM that is not doped by iodine and thus resistant to iodide/triiodide permeation.[18] Performing the same long-time voltage biasing test (Figure S22 in the Supporting Information), we find this device shows neither HTM doping nor halide segregation even up to 1.2 V, which supports our hypothesis that the oxidation of the organic HTM and permeation by iodide/triiodide plays a large role in facilitating halide segregation. Iodide transport through HTM may enable a lateral halide segregation, influenced by numerous other mass transport pathways, contributing to a complex final halide distribution.

It should be noted that the oxidation and reduction reactions need not exclusively occur at the physical anode (spiro-MeOTAD interface) and cathode (FTO interface). Due to the asymmetry in thermodynamic driving force (applied bias) as well as spatial inhomogeneity in morphology, local majority carrier type, and local concentration of reactant species, some regions will be more oxidizing (reducing) than other regions, which serve as the equivalent "anode" ("cathode"). Specifically, lattice iodide tends to be oxidized at those anode-like regions, and the oxidized iodine species will either diffuse or drift through the pathways described in Figure 5 from oxidizing to reducing regions and be returned to the lattice as iodide. At the same time, halide vacancies formed at the oxidizing regions will be filled by the sublattice halides consisting of both iodide and bromide (i.e., flux of vacancies away from where they are being created). In doing so, both sublattice iodide and bromide can migrate from "cathode" to "anode" via halide vacancies, but only electrochemically liberated iodine/triiodide/iodide can transport from "anode" to "cathode", the net effect being an unequal spatial redistribution of iodide and bromide and modification of local perovskite composition.

4. Conclusions

In summary, we have observed and quantified three voltage thresholds in an archetypal FTO/$MAPb(Br_xI_{1-x})$/(undoped) spiro-MeOTAD/Au halide perovskite device corresponding to spiro-MeOTAD doping, reversible halide segregation, and irreversible degradation. By systematically changing the ratio between iodide and bromide in the mixed-halide perovskite, we show that voltage-induced halide segregation can occur in all mixed-halide perovskite compositions, and the voltage

threshold for voltage-induced halide segregation is relatively constant across the composition range. Further analysis and discussion imply that the voltage thresholds observed in mixed iodide and bromide perovskite, which set the stability window of perovskite-based devices, are mainly determined by iodide/triiodide/iodine electrochemistry having the lower reaction potentials relative to bromide/tribromide/bromine. This study helps to reveal the origins of voltage-induced halide segregation in mixed-halide perovskites and leads to an improved understanding of electrochemical reactions and ion migration dictating the instability of perovskite-based devices under voltage bias.

5. Experimental Section

Materials and Solvents: Methylammonium iodide (MAI, > 99.99%) and methylammonium bromide (MABr, > 99.99%) were purchased from GreatCell Solar. PbI_2 (99.99%) was purchased from TCI. $PbBr_2$ (> 98%) was purchased from Alfa Aesar. Spiro-MeOTAD (> 99.5%) was purchased from Lumtec. PVK (average molecular weight ≈ 1100 000) was purchased from Sigma-Aldrich. Au (99.99%) was purchased from Kurt J. Lesker. DMF (anhydrous, 99.8%), DMSO (anhydrous, ≥ 99.9%) and CB (anhydrous, 99.8%) were purchased from Sigma-Aldrich. All materials and solvents were used as received.

Device Fabrication: $MAPbI_3$ (DMF), $MAPbI_3$ (DMSO), $MAPbBr_3$ (DMF), $MAPbBr_3$ (DMSO) stock solutions were prepared in a N_2-filled glovebox by dissolving PbI_2 (1 M) + MAI (1 M) in DMF or DMSO, $PbBr_2$ (1 M) + MABr (1 M) in DMF or DMSO. Then, the $MAPb(Br_xI_{1-x})_3$ precursor solution with $x \leq 0.6$ was prepared by mixing $MAPbI_3$ (DMF) and $MAPbBr_3$ (DMF) in a ratio of $(1-x) : x$. The $MAPb(Br_xI_{1-x})_3$ precursor solution with $x \geq 0.8$ was prepared by mixing $MAPbI_3$ (DMSO) and $MAPbBr_3$ (DMSO) in a ratio of $(1-x) : x$. Devices were fabricated on patterned FTO substrates (TEC 15, purchased from Xin Yan Technology Ltd.) that were ultrasonically cleaned with diluted detergent, deionized water, acetone, and isopropanol (IPA) in succession for 10 min. The as-cleaned FTO substrates were treated with O_2 plasma for 10 min prior to film deposition in a N_2-filled glovebox. The $MAPb(Br_xI_{1-x})_3$ precursor solution was spin-coated on the FTO substrates by a two-step program at 1000 rpm for 10 s with a ramping rate of 1000 rpm s^{-1}, and 6000 rpm for 30 s with a ramping rate of 2000 rpm s^{-1}. A solvent quenching step was performed 23 s (for the composition with $x \leq 0.6$) or 10 s (for the composition with $x \geq 0.8$) before the end of the whole spinning program by dropping 100 µL of CB on the center of spinning substrates. Then, the samples were immediately annealed on a hotplate at 100 °C for 60 min in a N_2-filled glovebox. Then, spiro-MeOTAD (85 mg mL^{-1} in CB) or PVK (25 mg·mL^{-1} in CB) solution was spin-coated on top of the perovskite layer at 2000 rpm for 45 s with a ramping rate of 2000 rpm s^{-1}. Finally, 100 nm Au was thermally evaporated on top of the spiro-MeOTAD layer in a vacuum chamber at pressure $<2 \times 10^{-6}$ Torr.

Characterization: The *J–t* and *J–V* curves were measured in the dark in a N_2-filled glovebox using a Keithley 2602B sourcemeter. PL spectra were measured by a fiber-coupled spectrograph equipped with a cooled Si charge-coupled device detector (Princeton Instruments, SpectraPro HRS-3000, and PIXIS 400B), excited by a 450 nm laser diode (Thorlabs, L450P1600MM) from the glass side. XPS spectra were measured by a Thermo-Scientific Kα X-ray Photoemission Spectrometer operating at a base pressure of 5×10^{-8} mbar and using an Al anode at a power of 72 W. SEM images were measured by an FEI Verios 460 XHR SEM. XRD patterns were measured by a Bruker D8 Discover X-ray diffractometer with a copper source and a wavelength of 1.54 Å. UV-vis absorption spectra were measured using an Agilent Technologies Cary 500 UV-Vis-NIR spectrometer. Cross-sectional STEM lamella samples were prepared by an FEI Helios NanoLab G3 UC DualBeam system. A Pt protection layer is deposited on top of the Au electrodes to avoid ion damage during STEM sample preparation. STEM images and EDX measurements were carried out in an FEI Talos F200X S/TEM, and all imaging was carried out in HAADF mode.

Supporting Information

Supporting Information is available from the Wiley Online Library or from the author.

Acknowledgements

The authors acknowledge funding for this work by the Department of the Navy, Office of Naval Research under ONR award number N00014-21-1-2767. This work was authored in part by the National Renewable Energy Laboratory, operated by Alliance for Sustainable Energy, LLC, for the U.S. Department of Energy (DOE) under Contract No. DE-AC36-08GO28308. Funding for R.A.K. was provided by the U.S. Department of Energy Office of Energy Efficiency and Renewable Energy, Solar Energy Technologies Office (SETO) project "De-risking Halide Perovskite Solar Cells" program (DE-FOA-0000990). The views expressed in the article do not necessarily represent the views of the DOE or the U.S. Government. The U.S. Government retains and the publisher, by accepting the article for publication, acknowledges that the U.S. Government retains a nonexclusive, paid-up, irrevocable, worldwide license to publish or reproduce the published form of this work, or allow others to do so, for U.S. Government purposes. The authors acknowledge the use of Princeton's Imaging and Analysis Center (IAC), which is partially supported by the Princeton Center for Complex Materials (PCCM), a National Science Foundation (NSF) Materials Research Science and Engineering Center (MRSEC; DMR-2011750).

Conflict of Interest

The authors declare no conflict of interest.

Data Availability Statement

The data that support the findings of this study are available from the corresponding author upon reasonable request.

Keywords

mixed-halide perovskites, voltage thresholds, voltage-induced halide segregation

Received: April 21, 2022
Published online: June 17, 2022

[1] A. Kojima, K. Teshima, Y. Shirai, T. Miyasaka, *J. Am. Chem. Soc.* **2009**, *131*, 6050.
[2] Z.-K. Tan, R. S. Moghaddam, M. L. Lai, P. Docampo, R. Higler, F. Deschler, M. Price, A. Sadhanala, L. M. Pazos, D. Credgington, F. Hanusch, T. Bein, H. J. Snaith, R. H. Friend, *Nat. Nanotechnol.* **2014**, *9*, 687.
[3] G. Xing, N. Mathews, S. S. Lim, N. Yantara, X. Liu, D. Sabba, M. Grätzel, S. Mhaisalkar, T. C. Sum, *Nat. Mater.* **2014**, *13*, 476.
[4] L. Dou, Y. Yang, J. You, Z. Hong, W.-H. Chang, G. Li, Y. Yang, *Nat. Commun.* **2014**, *5*, 5404.
[5] Y.-H. Kim, H. Cho, J. H. Heo, T.-S. Kim, N. Myoung, C.-L. Lee, S. H. Im, T.-W. Lee, *Adv. Mater.* **2015**, *27*, 1248.

[6] A. Sadhanala, S. Ahmad, B. Zhao, N. Giesbrecht, P. M. Pearce, F. Deschler, R. L. Z. Hoye, K. C. Gödel, T. Bein, P. Docampo, S. E. Dutton, M. F. L. De Volder, R. H. Friend, *Nano Lett.* **2015**, *15*, 6095.
[7] N. K. Kumawat, A. Dey, K. L. Narasimhan, D. Kabra, *ACS Photonics* **2015**, *2*, 349.
[8] K. Xiao, R. Lin, Q. Han, Y. Hou, Z. Qin, H. T. Nguyen, J. Wen, M. Wei, V. Yeddu, M. I. Saidaminov, Y. Gao, X. Luo, Y. Wang, H. Gao, C. Zhang, J. Xu, J. Zhu, E. H. Sargent, H. Tan, *Nat. Energy* **2020**, *5*, 870.
[9] A. Al-Ashouri, E. Köhnen, B. Li, A. Magomedov, H. Hempel, P. Caprioglio, J. A. Márquez, A. B. Morales Vilches, E. Kasparavicius, J. A. Smith, N. Phung, D. Menzel, M. Grischek, L. Kegelmann, D. Skroblin, C. Gollwitzer, T. Malinauskas, M. Jošt, G. Matič, B. Rech, R. Schlatmann, M. Topič, L. Korte, A. Abate, B. Stannowski, D. Neher, M. Stolterfoht, T. Unold, V. Getautis, S. Albrecht, *Science* **2020**, *370*, 1300.
[10] J. Xu, C. Boyd Caleb, J. Yu Zhengshan, F. Palmstrom Axel, J. Witter Daniel, W. Larson Bryon, M. France Ryan, J. Werner, P. Harvey Steven, J. Wolf Eli, W. Weigand, S. Manzoor, F. A. M. van Hest Maikel, J. Berry Joseph, M. Luther Joseph, C. Holman Zachary, D. McGehee Michael, *Science* **2020**, *367*, 1097.
[11] E. T. Hoke, D. J. Slotcavage, E. R. Dohner, A. R. Bowring, H. I. Karunadasa, M. D. McGehee, *Chem. Sci.* **2015**, *6*, 613.
[12] M. C. Brennan, A. Ruth, P. V. Kamat, M. Kuno, *Trends Chem.* **2020**, *2*, 282.
[13] A. J. Knight, L. M. Herz, *Energy Environ. Sci.* **2020**, *13*, 2024.
[14] I. L. Braly, R. J. Stoddard, A. Rajagopal, A. R. Uhl, J. K. Katahara, A. K. Y. Jen, H. W. Hillhouse, *ACS Energy Lett.* **2017**, *2*, 1841.
[15] Z. Xiao, L. Zhao, N. L. Tran, Y. L. Lin, S. H. Silver, R. A. Kerner, N. Yao, A. Kahn, G. D. Scholes, B. P. Rand, *Nano Lett.* **2017**, *17*, 6863.
[16] R. A. Z. Razera, D. A. Jacobs, F. Fu, P. Fiala, M. Dussouillez, F. Sahli, T. C. J. Yang, L. Ding, A. Walter, A. F. Feil, H. I. Boudinov, S. Nicolay, C. Ballif, Q. Jeangros, *J. Mater. Chem. A* **2020**, *8*, 242.
[17] R. A. Kerner, Z. Xu, B. W. Larson, B. P. Rand, *Joule* **2021**, *5*, 2273.
[18] R. A. Kerner, S. Heo, K. Roh, K. MacMillan, B. W. Larson, B. P. Rand, *ACS Energy Lett.* **2021**, *6*, 501.
[19] R. A. Kerner, L. Zhao, S. P. Harvey, J. J. Berry, J. Schwartz, B. P. Rand, *ACS Energy Lett.* **2020**, *5*, 3352.
[20] A. Merdasa, M. Bag, Y. Tian, E. Källman, A. Dobrovolsky, I. G. Scheblykin, *J. Phys. Chem. C* **2016**, *120*, 10711.
[21] D. Meggiolaro, S. G. Motti, E. Mosconi, A. J. Barker, J. Ball, C. Andrea Riccardo Perini, F. Deschler, A. Petrozza, F. De Angelis, *Energy Environ. Sci.* **2018**, *11*, 702.
[22] D. Meggiolaro, D. Ricciarelli, A. A. Alasmari, F. A. S. Alasmary, F. De Angelis, *J. Phys. Chem. Lett.* **2020**, *11*, 3546.
[23] Z. Ni, H. Jiao, C. Fei, H. Gu, S. Xu, Z. Yu, G. Yang, Y. Deng, Q. Jiang, Y. Liu, Y. Yan, J. Huang, *Nat. Energy* **2022**, *7*, 65.
[24] N. J. Jeon, J. H. Noh, W. S. Yang, Y. C. Kim, S. Ryu, J. Seo, S. I. Seok, *Nature* **2015**, *517*, 476.
[25] M. Saliba, T. Matsui, K. Domanski, J.-Y. Seo, A. Ummadisingu, M. Zakeeruddin Shaik, J.-P. Correa-Baena, R. Tress Wolfgang, A. Abate, A. Hagfeldt, M. Grätzel, *Science* **2016**, *354*, 206.
[26] D. Luo, W. Yang, Z. Wang, A. Sadhanala, Q. Hu, R. Su, R. Shivanna, F. Trindade Gustavo, F. Watts John, Z. Xu, T. Liu, K. Chen, F. Ye, P. Wu, L. Zhao, J. Wu, Y. Tu, Y. Zhang, X. Yang, W. Zhang, H. Friend Richard, Q. Gong, J. Snaith Henry, R. Zhu, *Science* **2018**, *360*, 1442.
[27] J. J. Yoo, G. Seo, M. R. Chua, T. G. Park, Y. Lu, F. Rotermund, Y.-K. Kim, C. S. Moon, N. J. Jeon, J.-P. Correa-Baena, V. Bulović, S. S. Shin, M. G. Bawendi, J. Seo, *Nature* **2021**, *590*, 587.
[28] L. Troian-Gautier, M. D. Turlington, S. A. M. Wehlin, A. B. Maurer, M. D. Brady, W. B. Swords, G. J. Meyer, *Chem. Rev.* **2019**, *119*, 4628.